

Self-reinforcement in filled rubber via strain-induced crystallisation

Received: 25 March 2025

Accepted: 14 August 2025

Published online: 02 September 2025



Tomohiro Miyata¹, Daisuke Watanabe², Shusuke Kanomi¹, Kai Chen¹, Wakana Miyoshi³, Tatsuya Kikuchi³, Takehiro Kitaura³, Toshihiro Kawakatsu⁴ & Hiroshi Jinnai¹✉

Strain-induced crystallisation in elastomers markedly increases their elastic moduli and rupture resistance. However, the mechanisms underlying this self-reinforcement in filled elastomers remain unclear owing to the nanoscale nature of the involved processes. Herein, isoprene rubber with/without silica nanoparticles is stretched to strains of >5 and concomitantly imaged via in situ transmission electron microscopy. Nanoscale electron diffraction mapping and in situ transmission electron microscopy results reveal that the self-reinforcement mechanism depends on the filler presence/absence. The unfilled isoprene rubber exhibits a spatially homogeneous strain-induced crystallisation behaviour resulting in drastic elastic modulus enhancement above the crystallisation onset strain. In contrast, the silica-filled isoprene rubber displays preferential crystallite formation in highly stressed regions along the silica aggregates aligned in the stretching direction. This reinforces the stress propagation pathways within the material and results in a lower crystallisation onset strain and higher rupture strength than those of the unfilled system. The insights on the role of fillers in determining strain-induced crystallisation phenomena and mechanical properties facilitate the rational design and development of elastomers.

Strain-induced crystallisation (SIC)^{1–5}, i.e., the formation of crystalline domains in stretched elastomers, imparts a unique self-reinforcement effect that increases the elastic moduli and rupture resistance, as these crystalline domains act as physical cross-links, strengthening the material only when mechanical strain and stress are applied. This phenomenon was discovered by Katz in 1925^{6,7} and has attracted the interest of researchers specialising in fundamental polymer physics and materials science^{5,8–10}. SIC in natural rubber (NR) and isoprene rubber (IR), both based on *cis*-1,4-polyisoprene (PI), has been extensively investigated^{11–19} because of their importance in high-performance applications ranging from automotive tyres to vibration isolation systems in precision equipment²⁰. Recent investigations have revealed that SIC manifests locally at void edges and crack tips,

arresting crack propagation^{21–23}. A recent breakthrough has expanded the scope of this phenomenon by demonstrating that SIC also occurs in gel systems, resulting in remarkable toughening and almost fully reversible mechanical properties^{3,4}. The appropriate utilisation of SIC can markedly contribute to the development of materials with tailored mechanical responses and sustainable manufacturing through the creation of durable materials with less raw material input.

According to Flory, SIC is largely driven by the reduction in the conformational entropy of polymer chains during stretching, because it facilitates the transition from an amorphous state to a crystalline one (the entropy change for crystallisation is smaller than that for the unstretched state)^{24,25}. This fundamental work has triggered extensive research on SIC mechanisms and the properties of

¹Institute of Multidisciplinary Research for Advanced Materials, Tohoku University, Sendai, Miyagi, Japan. ²Department of Applied Chemistry, Graduate School of Engineering, Tohoku University, Sendai, Miyagi, Japan. ³Sumitomo Rubber Industries, Ltd, Kobe, Hyogo, Japan. ⁴Department of Physics, Graduate School of Science, Tohoku University, Sendai, Miyagi, Japan. ✉e-mail: hiroshi.jinnai.d4@tohoku.ac.jp

the resulting materials^{8,9,26}. The morphological characteristics of the nuclei and crystallites formed during stretching, which are crucial for the thermodynamic and kinetic theories of SIC, have also been studied^{27–30}. Yeh and Hong demonstrated that the strain-induced crystallites in vulcanised IR are constrained by cross-links to form fibrillar or oriented twisted lamellar structures with dimensions of <30 nm²⁸. Gros et al.³⁰ rationalised fast time-resolved wide-angle X-ray diffraction (WAXD) data²⁹ and suggested that the formation of bundle-like nuclei during stretching reduces the surface free energy, which may be a more important mechanism for nucleation than entropy reduction suggested by Flory³⁰.

Technological advances have enabled increasingly detailed analyses of the spatial distribution of strain-induced crystals. Atomic force microscopy (AFM) has been used to map elastic modulus in stretched rubber with a spatial resolution of tens of nanometres, revealing the formation of nanoscale fibrillar regions with higher elastic modulus in unfilled rubber^{31,32}. Microfocused scanning X-ray diffraction (m-SXRD) has also been used to map WAXD patterns on a micrometre scale. These investigations have demonstrated that SIC occurs locally at void edges and crack tips, hindering crack propagation at strains smaller than that of SIC onset in unfilled rubber^{21–23}.

Studies have been extended to filled elastomers, particularly nanofiller-containing NR and IR, which are crucial for industrial applications because of their enhanced moduli and superior rupture strengths^{20,33}. WAXD studies have revealed that nanofillers (e.g., carbon black and silica) reduce both the SIC onset strain and crystallite orientation degree^{34–36}. However, understanding the microscopic origins of the interplay between fillers and SIC remains challenging because of the need to simultaneously visualise the nanoscale fillers and strain-induced crystals under large deformations. Although AFM exhibits a high spatial resolution, the correlation between the high-modulus regions observed by AFM and the spatial distribution of strain-induced crystals requires further verification. Unlike AFM, m-SXRD provides direct crystallographic information but has a spatial resolution insufficient for the simultaneous visualisation of nanoscale fillers and strain-induced crystals; hence, the fundamental SIC mechanisms in filled systems are underexplored.

We have recently developed transmission electron microscopy (TEM) techniques for observing structural deformation in stretched and sheared rubbers^{37–39}. Moreover, an advanced imaging approach based on nanoscale electron diffraction (ED) for semicrystalline polymers has been established by Panova et al.⁴⁰, and has since been applied to organic semiconductors⁴¹, polyolefins^{42,43}, and other semicrystalline polymers^{44–46}. This technique relies on specimen scanning with a nanoscale electron beam and ED pattern collection at different points to reconstruct two-dimensional crystal distribution maps from pattern intensities. These maps provide a spatial resolution nearly three orders of magnitude higher than that of m-SXRD, enabling the precise visualisation of nanocrystals in semi-crystalline polymers. Herein, we integrate two cutting-edge electron microscopy techniques, namely, in situ deformation TEM and nanoscale ED mapping, to elucidate the spatial arrangement of strain-induced crystallites in filled and unfilled rubbers, providing nanoscopic insights into the interplay between fillers and SIC and establishing correlations between microscopic phenomena and macroscopic mechanical properties.

Results and discussion

Mechanical property–crystallinity relation

IR filled with silica nanoparticles (20 parts per hundred rubber (phr)) and unfilled IR were prepared to investigate the interplay between internal structure and SIC behaviour. The stress–strain (S–S) curves of the two specimens revealed distinct mechanical behaviours (Fig. 1a). The unfilled IR showed a sharp stress rise at a tensile strain (ε) of ≈ 4 , whereas the silica-filled IR exhibited a gradual stress increase and markedly higher rupture strength.

The tensile strain–dependent intensity of the 200 WAXD peak of PI crystals (Fig. 1b, c), which is proportional to crystallinity, revealed that the unfilled and silica-filled IR exhibited different crystallisation kinetics. The unfilled IR displayed a steep crystallinity increase starting from $\varepsilon \approx 3.5$, whereas the silica-filled IR showed a more gradual rise initiating at a lower strain ($\varepsilon \approx 2.0$). These differences are clearly visible in the original 2D-WAXD patterns, as shown in Supplementary Fig. 1. These crystallinity profiles well matched the stress increases observed in the S–S curves (Fig. 1a). Notably, the stress of the unfilled IR began to rise at $\varepsilon \approx 4$ following the onset of the crystallinity increase at $\varepsilon \approx 3.5$, which suggested that SIC considerably contributed to stress enhancement. Although WAXD provides valuable information on spatially averaged SIC behaviour, the understanding of SIC in filled systems remains phenomenological due to the lack of insights into the underlying microscopic mechanisms.

TEM of stretched unfilled IR

The TEM images of the unfilled IR were acquired during tensile deformation up to $\varepsilon = 5.8$, a value comparable with the failure strain observed in macroscopic tensile tests, and featured dark areas in the bright rubber matrix (Fig. 1d). These areas were identified as vulcanisation promoters, specifically ZnO particles and stearic acid aggregates. With the increasing strain, the additives progressively separated along the stretching direction. The realisation of such a large deformation ($\varepsilon \approx 6$) suggested that the damage induced by the electron beam was minimal.

ED mapping of stretched unfilled IR

Scanning transmission electron microscopy (STEM) and nanoscale ED mapping were conducted to analyse the unfilled IR stretched to $\varepsilon = 5.8$ (Fig. 2a). Figure 2b shows an annular dark-field (ADF)-STEM image of the region highlighted in Fig. 1d (yellow rectangle). This image exhibits a contrast inverse to that of the corresponding TEM image, with the ZnO particles and stearic acid aggregates appearing as bright features.

Nanoscale ED patterns were acquired in 40×40 nm regions within the area shown in Fig. 2b (purple rectangle) and referred to as 40 nm ED patterns (Fig. 2c). Diffraction spots (yellow triangles) were observed in several of these patterns, although the low electron dose complicated the differentiation between these spots and background (BG) noise. The 200 nm ED pattern generated by integrating the twenty five 40 nm ED patterns in Fig. 2c exhibited pronounced diffraction spots corresponding to the {200}, {201}, {120}, and {002} planes of the PI crystals (200, 201, 120, and 002 spots, respectively; Fig. 2d) and was consistent with the integrated ED pattern obtained from the entire field of view in Fig. 2b (Fig. 2e), specifically from the rubber matrix region, excluding the stearic acid aggregates (Supplementary Fig. 2). The 200/201 and 120 spots cannot be simultaneously detected in any single PI crystal (Supplementary Fig. 3). Thus, the occurrence of these spots in the single 200 nm ED pattern indicated the coexistence of multiple crystallites with diverse orientations within 200×200 nm areas. In these areas, the *c*-axes of the PI crystallites (i.e., the PI chain directions) were mostly aligned parallel to the stretching direction while maintaining rotational variance around their corresponding *c*-axes.

Unlike the ED patterns integrated over broad regions, the individual 40 nm ED patterns (Fig. 2c) displayed 200, 201, or 120 spots. The fact that not all spots appeared simultaneously suggested that the number of crystallites within each 40 nm area was insufficient to incorporate all possible orientations. The number of crystallites within the measured volume (N_C) was estimated using the relationship $N_C = \chi_C V_{ED}/V_C$, where χ_C represents the crystallinity at $\varepsilon = 5.8$ estimated by WAXD ($\approx 7\%$), V_{ED} denotes the volume measured by ED (40×40 nm area with a specimen thickness of 60 nm at $\varepsilon = 5.8$), and V_C corresponds to the dimensions of individual PI crystallites ($5 \times 5 \times 10$ nm, as previously reported¹⁹). This calculation yielded $N_C \approx 27$.

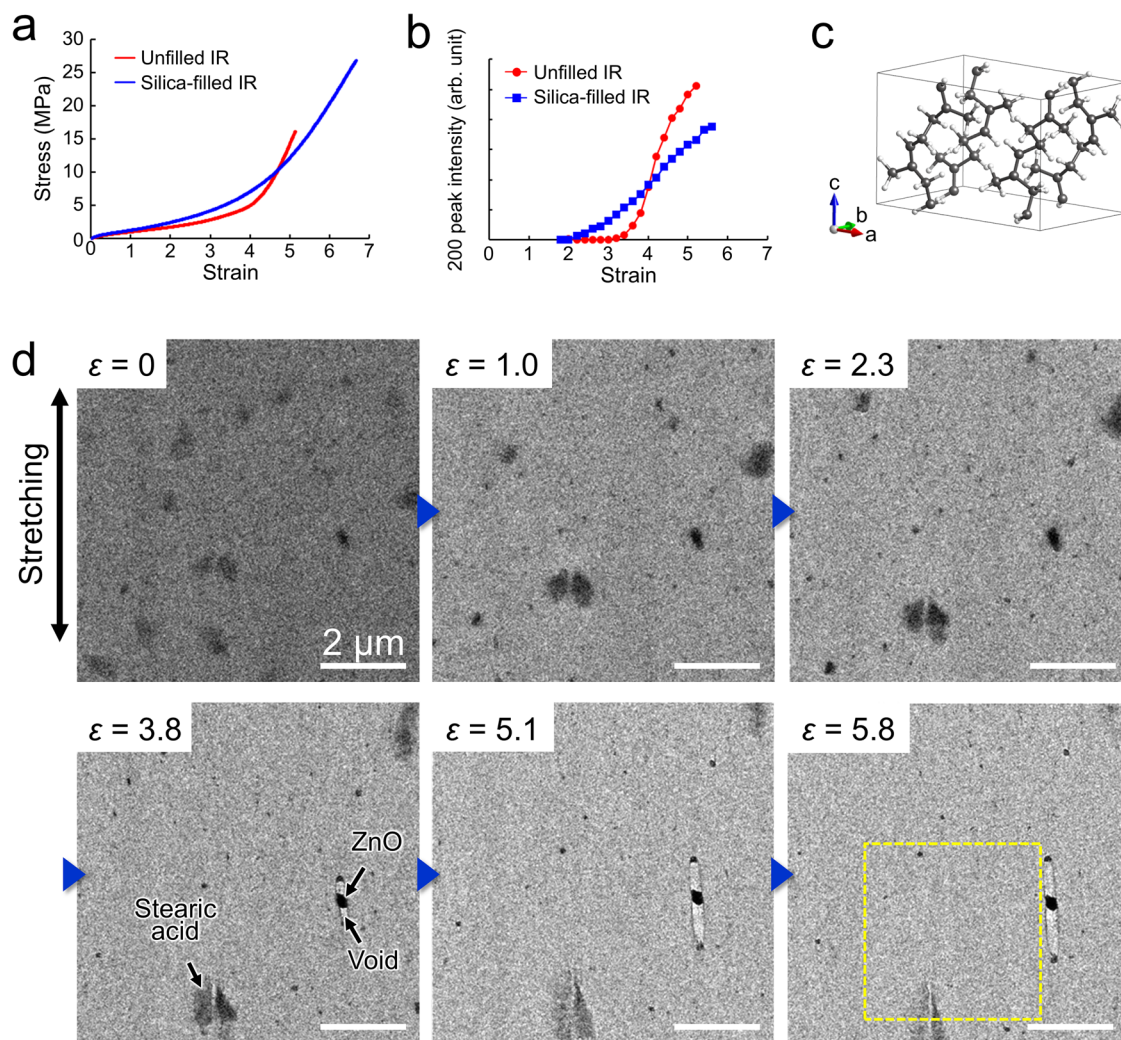


Fig. 1 | Fundamental information on the isoprene rubber (IR) specimens and in situ tensile transmission electron microscopy (TEM) images of the unfilled IR. a Stress–strain curves of the unfilled (red) and silica-filled (blue) specimens. **b** Tensile-strain-dependent intensity of the 200 wide-angle X-ray

diffraction (WAXD) peak for the unfilled (red circles) and silica-filled (blue squares) IR. **c** Crystal structure of *cis*-1,4-polyisoprene (PI). **d** TEM images captured during the stretching of the unfilled IR at tensile strains (ϵ) of 0, 1.0, 2.3, 3.8, 5.1, and 5.8. Black arrows indicate the stretching direction.

The average number of crystallites detectable via 200 spots in individual 40 nm ED patterns ($N_{c,det}$) was calculated as $N_{c,det} = N_C P_{200spot}$, where $P_{200spot}$ represents the probability of observing 200 spots in an ED pattern from PI crystallites randomly oriented around their *c*-axis as explained ($\approx 2.5\%$, as detailed in Supplementary Fig. 3). Consequently, $N_{c,det}$ was calculated to be approximately 0.7. This result strongly suggested that each observed diffraction spot within these 40 nm ED patterns was due to a single crystallite.

Crystallite map of stretched unfilled IR

The spatial distribution of the strain-induced crystallites was analysed using 40 nm ED patterns, which provided information on individual crystallites. To distinguish diffraction spots from BG intensity containing noise, two (BG and maximum intensity) histograms were constructed using a circular mask located at a magnitude of scattering vector (*s*, see Methods for definition) of 1.6 nm^{-1} , corresponding to the *s* for 200 spots (inset, Fig. 2f). (i) The BG histogram was constructed from integrated intensities within the circular mask for each ED pattern, with measurements performed at 1° intervals over the angular range $\varphi = -90^\circ$ to -60° and 60° to 90° (Fig. 2f and Supplementary Fig. 4a). The BG histogram, representing the intensity distribution at

positions devoid of the 200 spots, facilitated the discrimination between these spots and BG intensity containing noise in the ED patterns. (ii) The maximum intensity histogram was constructed from the highest integrated intensities within the circular mask for each ED pattern across the angular range $\varphi = -90^\circ$ to 90° (Fig. 2f and Supplementary Fig. 4a). This histogram characterised the intensities of 200 spots.

Crystallite positions exhibiting 200 spots were discriminated from BG intensity containing noise with 99.9% statistical confidence by selecting 40 nm ED patterns where the maximum intensities exceeded the 99.9th percentile of the BG histogram. The crystallites identified via 200 spots in 40 nm ED patterns were almost uniformly distributed across the field of view (Fig. 2g), which suggested the uniformity of environmental conditions throughout the specimens.

TEM of stretched filled IR

Figure 3 presents the TEM images of silica-filled IR recorded under tensile deformation up to $\epsilon = 5.3$, showing dark silica nanoparticle aggregates dispersed in the bright rubber matrix. These images reveal that the aggregates stretched and/or split in the stretching direction under large deformations and were therefore correspondingly aligned.

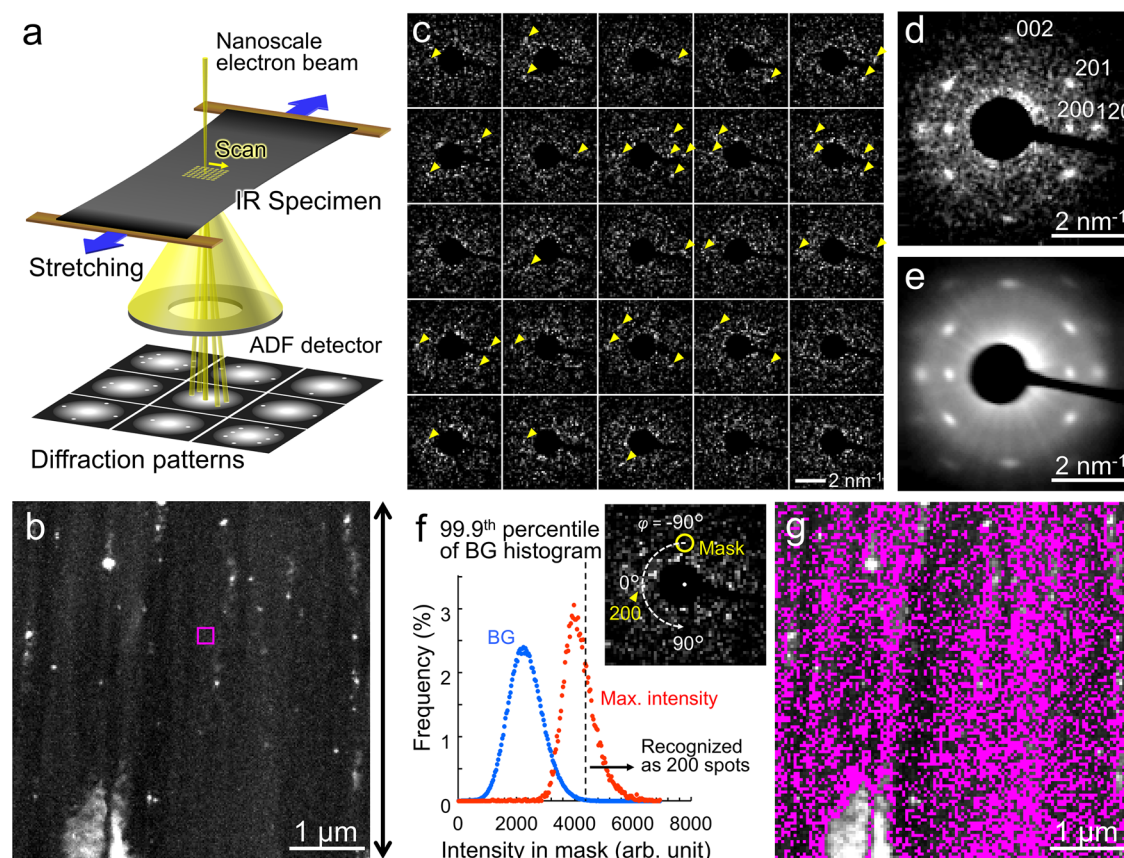


Fig. 2 | Nanoscale electron diffraction (ED) mapping of the stretched unfilled IR. **a** Schematic of the annular dark-field scanning transmission electron microscopy (ADF-STEM) imaging and nanoscale ED mapping system. **b** ADF-STEM image of the boxed area in Fig. 1d ($\epsilon = 5.8$). The black arrow indicates the stretching direction. **c** ED patterns obtained from the purple-box-enclosed region in (b). Each pattern was measured over an area of 40×40 nm. **d** ED pattern integrated over an area of

200×200 nm, corresponding to the twenty-five 40 nm ED patterns in (c). **e** Diffraction pattern integrated across the entire rubber region in (b). **f** Background and maximum intensity histograms for crystallite detection using 200 spots in 40 nm ED patterns. **g** Spatial distribution of the strain-induced crystallites detected using 200 spots.

Crystallite map of stretched filled IR

Figure 4a presents the ADF-STEM image corresponding to the boxed area in the TEM image of the filled IR captured at $\epsilon = 5.3$ (Fig. 3), with the silica aggregates appearing white in the dark rubber matrix. This image exhibits an alternating arrangement of silica-rich and silica-poor columns parallel to the stretching direction. This is the first study to uncover such columnar arrangements under large deformation conditions (up to $\epsilon = 5.3$).

Furthermore, the rubber regions between these stretch-aligned aggregates exhibit a bright contrast in the ADF-STEM image, suggesting that the rubber in these regions has either a higher density or larger thickness. This structure may arise from the SIC behaviour and inhomogeneous strain/stress distributions, as discussed below.

Figure 4b, c shows the 40 nm ED patterns acquired in regions 1 and 2 of Fig. 4a, respectively. The ED patterns in region 1 exhibit the 200, 201, and 120 spots of PI crystallites, whereas those in region 2 show few diffraction spots. This contrast indicates the coexistence of crystallite-rich and crystallite-poor domains within the stretched specimen. The integrated 200 nm ED patterns acquired in regions 1 and 2 (Fig. 4d, e, respectively) corroborate this heterogeneous crystallite distribution. Such a heterogeneous distribution is unrecognisable in the average ED pattern acquired across the entire rubber region (Fig. 4f).

Figure 4g illustrates the spatial distribution of crystallites determined from the intensities of the 200 spots in 40 nm ED patterns (Supplementary Fig. 4). Locations with 200 spot intensities exceeding

the 99.9th percentile of BG intensities are highlighted in the ADF-STEM images. Strain-induced crystallites preferentially formed along the silica-rich columns, whereas silica-poor columns exhibited fewer crystallites. A similar distribution pattern was obtained using 120 spot intensities (Supplementary Fig. 6), corroborating the results of the 200-spot-based analysis (Fig. 4g). The presence of both the 200 and 120 spots in the silica-rich columns suggested that crystallites with various *c*-axis orientations coexisted in these regions.

Relationship between crystallite distribution and local strain/stress

Local strain distributions were analysed by tracking characteristic points in the TEM images acquired at $\epsilon = 0.8$ –5.3 (Fig. 3), as reported previously³⁸. The maps of local maximum and minimum principal strains (ϵ_{\max} and ϵ_{\min} , respectively), as shown in Fig. 5b and Supplementary Fig. 7b, indicate a non-uniform nanoscale deformation behaviour, which is attributed to the heterogeneous distribution of silica aggregates. Crystallite locations were overlaid on these maps, as shown in Fig. 5e and Supplementary Fig. 7c. Furthermore, the histogram in Supplementary Fig. 7a illustrates the quantitative correlation between the distributions of local ϵ_{\max} and crystallites. This quantitative analysis revealed that the local ϵ_{\max} at locations where strain-induced crystallites exist tends to be smaller than the average strain, suggesting that regions with dense strain-induced crystallites become less deformable than those with sparse crystallites due to an increased local elastic modulus.

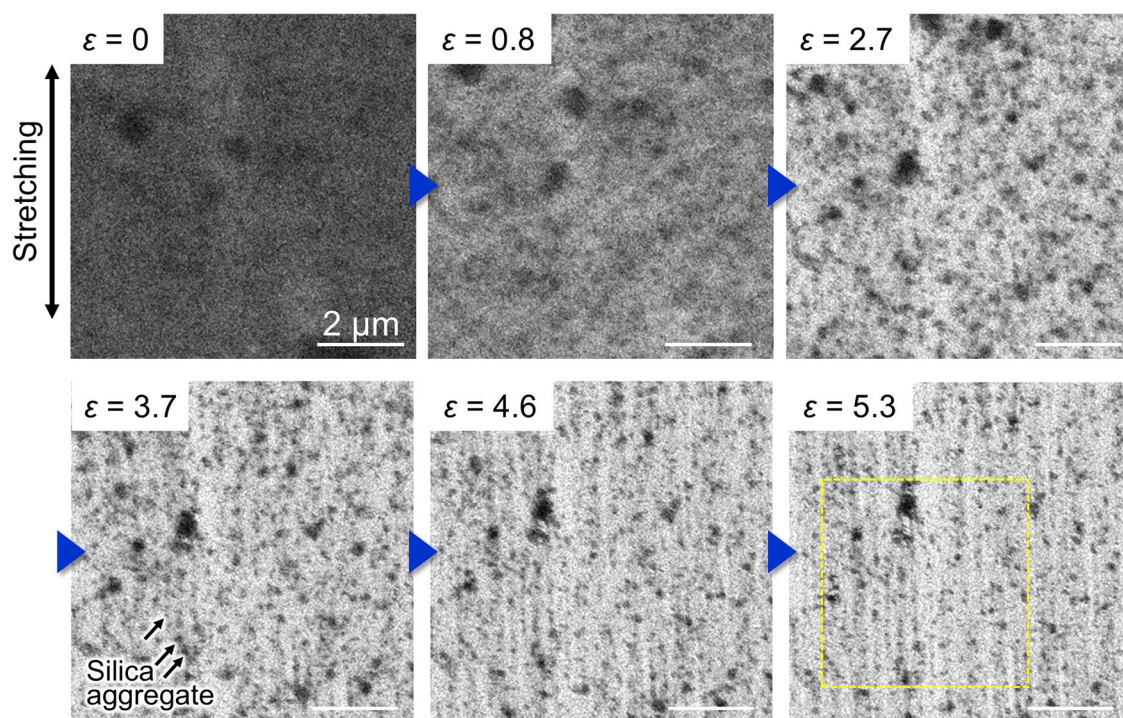


Fig. 3 | TEM images of the filled IR stretched to different strains. The black arrow indicates the stretching direction.

Subsequently, to estimate local stress distribution in the stretched silica-filled IR, we performed finite element method (FEM) simulations of tensile deformation based on the spatial distribution of silica aggregates in the TEM image at $\varepsilon = 5.3$. The map of the local normal stress in the stretching direction (Fig. 5c) indicated that substantial stress propagated along the silica aggregates aligned in this direction. This stress distribution was well correlated with the observed crystallite distribution (Fig. 5f). Thus, the aligned silica aggregates were concluded to enhance local stress in interstitial rubber regions, promoting site-specific crystallite formation. These crystallites, in turn, reinforced the columnar arrangements of the silica aggregates, serving as principal stress propagation pathways.

Self-reinforcement mechanisms based on SIC in unfilled and filled IR

In the unfilled IR with a relatively uniform environment, SIC begins uniformly throughout the specimen at a threshold of $\varepsilon \approx 3.5$, and the crystallinity steeply increases beyond this point (Fig. 1b), which results in a sharp stress increase (Fig. 1a).

In the silica-filled IR, silica aggregates align to form silica-rich columns upon stretching, which serve as stress propagation pathways by bearing substantial stress. Site-specific SIC occurs along the aligned silica columns, enhancing the elastic moduli of the stress propagation pathways, as illustrated in Fig. 6. This localised reinforcement increases the macroscopic elastic modulus and rupture strength (Fig. 1a). The earlier onset of SIC ($\varepsilon \approx 2.0$) compared with that in the unfilled IR ($\varepsilon \approx 3.5$) and gradual increase in crystallinity (Fig. 1b) are attributed to the substantial heterogeneity of local strain.

Our findings reveal fundamental differences in the reinforcement mechanisms of the unfilled and filled systems. The unfilled systems exhibit uniform self-reinforcement via SIC, whereas filled systems demonstrate preferential SIC reinforcement along filler-mediated stress propagation pathways (Fig. 6). This study highlights the crucial role of filler arrangement in controlling the mechanical properties of crystallisable elastomers, thereby providing essential insights for material design.

Methods

Material preparation

The unfilled IR comprised IR (100 phr; Nipol IR2200, ZEON Corporation, Japan), ZnO (3 phr), stearic acid (2.5 phr), sulphur (3 phr), and a vulcanisation accelerator (*N*-cyclohexyl-2-benzothiazole sulfenamide). The filled IR additionally contained silica nanoparticles with a diameter of 17–18 nm (20 phr; ULTRASIL VN3, Evonik Industries AG, Germany) and a silane coupling agent (1.6 phr; Si266, Evonik Industries AG, Germany). The formulations were vulcanised at 150 °C for 35 min.

Mechanical property test

Dumbbell-shaped specimens (ISO 37 Type 1A) were cut from 2 mm-thick rubber sheets. Uniaxial tensile tests were conducted at room temperature using a fully automated rubber tensile testing machine (Strograph AE2, Toyo Seiki Seisaku-sho, Ltd, Japan) at a cross-head speed of 500 mm min⁻¹ (Fig. 1a). Tensile strain was calculated by measuring the distance between gauge marks.

WAXD measurements

WAXD experiments were conducted using a SmartLab instrument (Rigaku Corporation, Japan) equipped with a Cu K_{α} X-ray source ($\lambda = 1.5405 \text{ \AA}$) and PILATUS-100K detector (DECTRIS AG, Switzerland). The specimen-to-detector distance was 149.16 mm. The specimens were scanned at a rate of $2\theta = 0.01^\circ$ per step and 0.06 s per step to obtain two-dimensional WAXD patterns. The dumbbell-shaped specimens (ISO 37 Type 4) had thicknesses of 0.5 mm (unfilled IR) and 0.3 mm (silica-filled IR). After measurements at a tensile strain of $\varepsilon = 0$, the unfilled and silica-filled IR specimens were stretched to $\varepsilon = 2$ and 1.4, respectively, and then elongated in 20% increments until rupture, which occurred at $\varepsilon = 5.4$ and 5.6, respectively. For each strain, WAXD measurements were conducted for ~5 min. The thicknesses of the elongated specimens were calculated using a Poisson's ratio of 0.5, and the WAXD data were thickness-corrected.

The WAXD intensities in the areas including 200, 120, and 201 diffraction peaks were averaged along the azimuthal direction to produce one-dimensional scattering intensity- q profiles (azimuthal

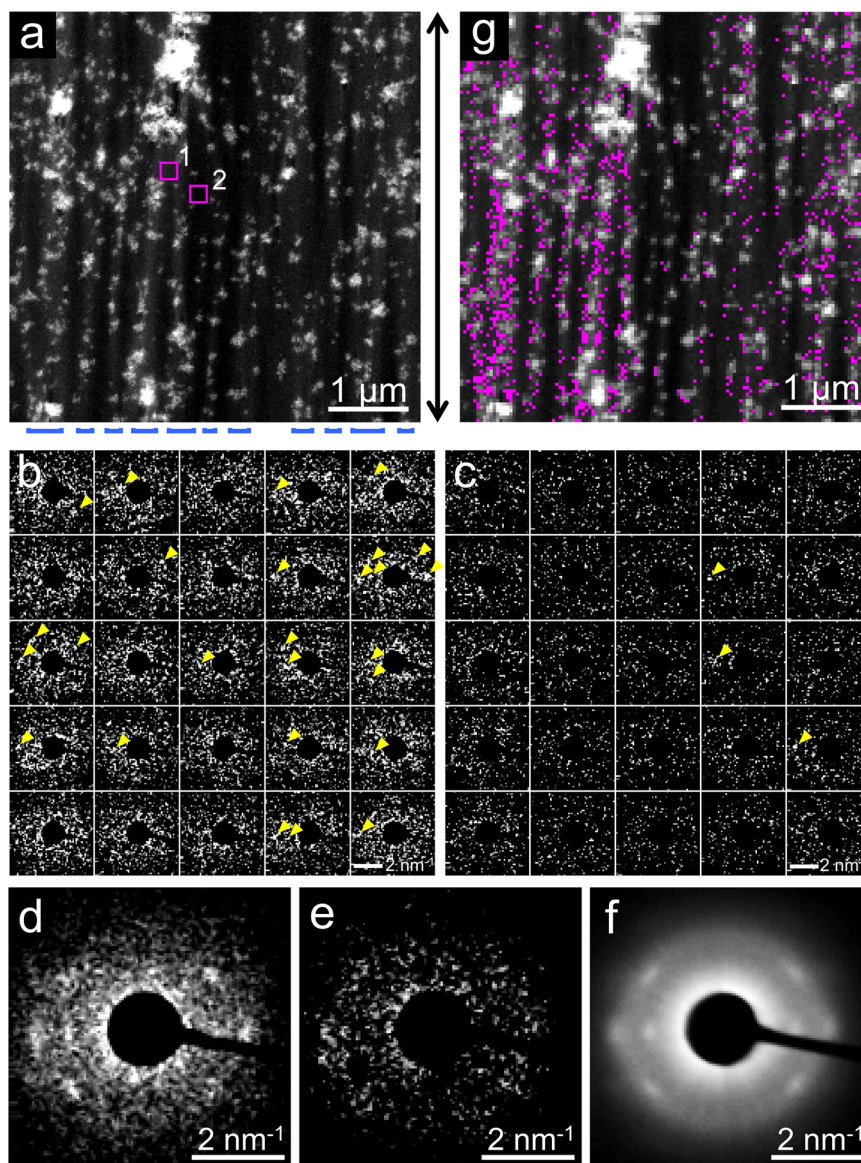


Fig. 4 | Nanoscale ED mapping of the stretched silica-filled IR. **a** ADF-STEM image of the boxed area in Fig. 3 ($\varepsilon = 5.3$). The black arrow indicates the stretching direction. Silica-rich columns are indicated by blue brackets below the image. **b, c** 40 nm ED patterns obtained from regions 1 and 2 in (a), respectively. **d, e** 200 nm

ED patterns integrated over the areas shown in (b) and (c), respectively. **f** ED pattern integrated across the entire rubber region in (a). **g** Spatial distribution of crystallites determined from the intensity of the 200 spots in the corresponding 40 nm ED patterns. Scale bars for (b, c) represent $s = 2 \text{ nm}^{-1}$.

angle: $70^\circ < \varphi < 110^\circ$ for 200 and 120 peaks and $40^\circ < \varphi < 75^\circ$, $105^\circ < \varphi < 140^\circ$ for 201 peaks), where q is the scattering vector ($q = 4\pi \sin \theta / \lambda$; 2θ : scattering angle ($^\circ$)). The total scattering intensity of stretched specimens was assumed to be similar to that of unstretched specimens. A Gaussian function was used to fit the peaks in the one-dimensional profiles and thus separate the diffraction peaks from the amorphous halo. The areas of the 200 diffraction spots were used to evaluate the increase in the crystal amount (Fig. 1b).

In situ tensile TEM imaging

The IR samples were cut into ~400 nm-thick films using a cryo-ultramicrotome (EM UC7, Leica Microsystems GmbH, Germany) at -160°C . A fine probe was used to move the sample onto the cartridge of the tensile TEM holder (Mel-Build Co., Japan), and the ends of the film were fixed to the cartridge with an adhesive to prevent peeling off under stretching. The cartridge had a 30 μm gap that could be opened

symmetrically and stably so that the specimen films were stretched uniformly.

A cartridge with the specimen film was mounted on a tensile TEM holder, and the stretching process was observed using a transmission electron microscope (JEM-F200, JEOL Ltd, Japan) equipped with a K3 IS camera (Gatan, Inc., USA). The specimens were stretched in a stepwise manner and observed at $\varepsilon = 0, 1.0, 2.3, 3.2, 3.8, 5.1$, and 5.8 for the unfilled IR and $\varepsilon = 0, 0.8, 1.8, 2.7, 3.7, 4.6$, and 5.3 for the silica-filled IR. The thickness decreased from ~400 nm at $\varepsilon = 0$ to 60 nm at $5 < \varepsilon < 6$. The accelerating voltage was 200 kV, and the image resolution was 7.1 nm pix^{-1} . The electron dose was $0.002 \text{ e } \text{\AA}^{-2}$ per image. The average strain was estimated by tracking two characteristic points located at both ends of the field of view during stretching. The specimens were deformed in a planar stretching mode, i.e., the specimen width (dimension perpendicular to the stretching direction) was maintained, whereas the thickness decreased upon stretching. The specimen thickness was inversely proportional to the stretching ratio ($1 + \varepsilon$).

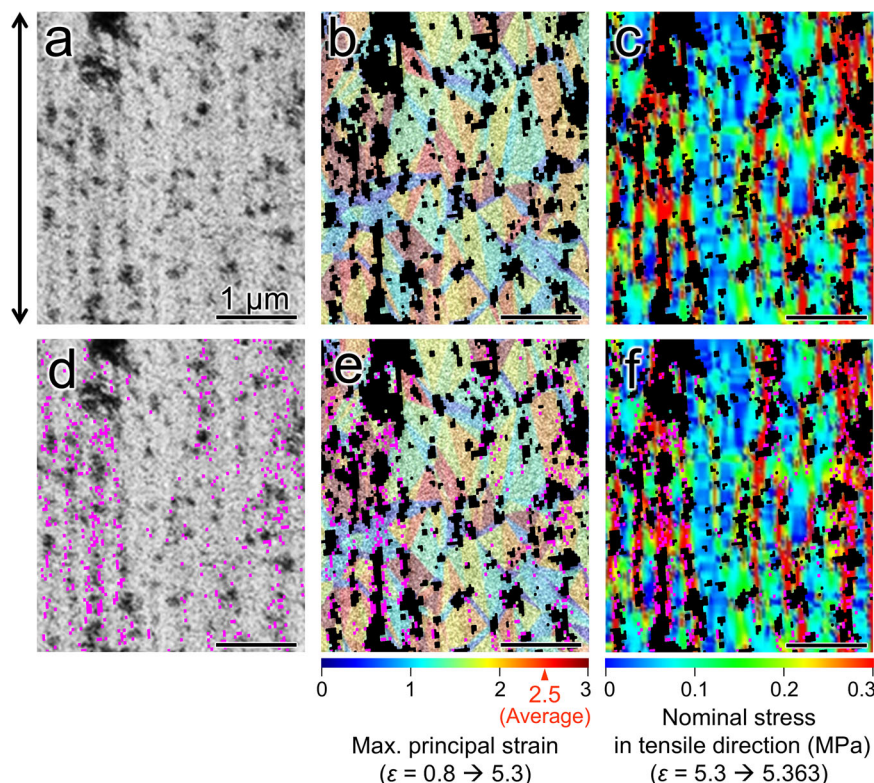


Fig. 5 | Relationship between the spatial distribution of crystallites and local strain/stress fields. **a** Enlarged TEM image of the boxed region in Fig. 3 ($\varepsilon = 5.3$). The black arrow indicates the stretching direction. **b** Colour map of local ε_{\max} in the TEM image of **(a)** estimated by tracking the displacements of characteristic points from $\varepsilon = 0.8$ – 5.3 . These local strain distributions do not fully reflect the history of the local strains from $\varepsilon = 0$. The tensile strain for $\varepsilon = 0.8$ – 5.3 is 2.5, as indicated on

the colour bar. **c** Spatial distribution of normal stress in the stretching direction estimated by the finite element method (FEM) simulation. **d–f** Locations of crystallites identified from the intensities of the 200 spots (indicated by pink dots). (**d–f**) correspond to **(a–c)**, respectively. Colour bars for **(b, e)** and **(c, f)** are displayed at the bottom.

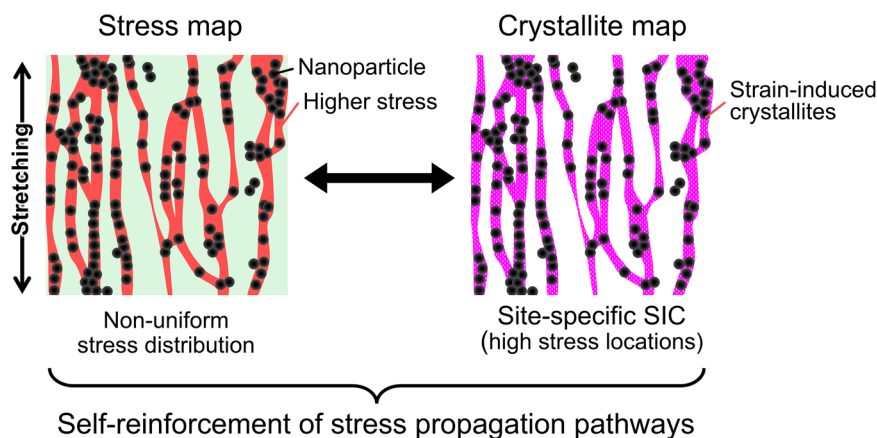


Fig. 6 | Proposed self-reinforcement mechanism via SIC of the silica-filled IR. Coincidence between the local stress and crystalline maps indicates that strain-induced crystallites are formed along the stress propagation pathways in filled rubber, resulting in further reinforcement of the stress propagation pathways.

Estimation of local strain distribution

To analyse the distributions of the local maximum and minimum principal strains (ε_{\max} and ε_{\min} , respectively) in the TEM images of the silica-filled IR, we tracked characteristic points in these images as described elsewhere³⁸. Owing to the difficulty in recognising fillers and characteristic points in the TEM image at $\varepsilon = 0$ due to the specimen thickness, the point tracking and strain calculation commenced at $\varepsilon = 0.8$ and not 0. Thus, the net strain calculated from $\varepsilon = 0.8$ – 5.3 was 2.5, which appeared as the average strain in the map of the local ε_{\max} . The Delaunay triangulation method⁴⁷ was applied to the point distribution

of the final image ($\varepsilon = 5.3$) to divide it into triangular elements. Point linkages and triangular elements were applied to the other images.

The ε_{\max} and ε_{\min} of the large deformed triangular elements were calculated using the following procedure. The right stretch tensor \mathbf{U} , which represents the pure stretch component of the deformation excluding rigid-body rotation, was derived from the deformation gradient tensor \mathbf{F} as

$$\mathbf{U}^2 = \mathbf{C} = \mathbf{F}^T \mathbf{F} = \left(\frac{d\mathbf{x}}{d\mathbf{X}} \right)^T \left(\frac{d\mathbf{x}}{d\mathbf{X}} \right),$$

where \mathbf{C} is the right Cauchy–Green deformation tensor, and \mathbf{X} and \mathbf{x} are the coordinates before and after the deformation, respectively. The diagonalisation of \mathbf{U} yielded \mathbf{U}_{dia} as

$$\mathbf{U} = \begin{pmatrix} U_{11} & U_{12} \\ U_{21} & U_{22} \end{pmatrix} \mapsto \mathbf{U}_{\text{dia}} = \begin{pmatrix} \lambda_1 & 0 \\ 0 & \lambda_2 \end{pmatrix},$$

with the eigenvalues λ_1 and λ_2 given by

$$\lambda_1, \lambda_2 = \frac{U_{11} + U_{22} \pm \sqrt{(U_{11} - U_{22})^2 - 4U_{12}U_{21}}}{2}.$$

The Biot strain tensor \mathbf{B} was calculated as

$$\mathbf{B} = \begin{pmatrix} \varepsilon_1 & 0 \\ 0 & \varepsilon_2 \end{pmatrix} = \mathbf{U}_{\text{dia}} - \mathbf{I} = \begin{pmatrix} \lambda_1 - 1 & 0 \\ 0 & \lambda_2 - 1 \end{pmatrix}.$$

ε_{max} and ε_{min} were subsequently determined as $\varepsilon_{\text{max}} = \max(\varepsilon_1, \varepsilon_2)$ and $\varepsilon_{\text{min}} = \min(\varepsilon_1, \varepsilon_2)$.

ADF-STEM and nanoscale ED analyses

Specimens stretched to the desired strain ($\varepsilon = 5.8$ for the unfilled IR and 5.3 for the silica-filled IR) were imaged via ADF-STEM, and nanoscale ED mapping was performed using a STELA camera (Gatan, Inc., USA). An electron beam with a convergence angle of 0.19 mrad and calculated diameter of 9.8 nm (full width at half maximum (FWHM)) was used to scan a $5 \times 5 \mu\text{m}$ area with a pixel size of $20 \times 20 \text{ nm}$. The probe current and pixel time were $5.0 \times 10^7 \text{ e}^- \text{ s}^{-1}$ and 0.005 s, respectively. The electron doses averaged for each pixel ($20 \times 20 \text{ nm}$) and electron probe (FWHM diameter = 9.8 nm) were determined as $6.3 \text{ e}^- \text{ \AA}^{-2}$ and $34 \text{ e}^- \text{ \AA}^{-2}$, respectively. The detection angle range of the ADF detector was 17–62 mrad. The STELA camera acquired the ED pattern for each pixel. To enhance the signal-to-noise ratio for subsequent analysis, ED patterns from $40 \times 40 \text{ nm}$ areas were constructed by integrating the four ED patterns originally collected from $20 \times 20 \text{ nm}$ areas. The crystal distribution was analysed in the presence of the 200 diffraction spots of PI in the ED patterns.

Strain-induced crystallite mapping

The distribution of strain-induced crystallites was characterised as follows.

- A circular mask with a diameter of $s = 0.36 \text{ nm}^{-1}$ ($s = \sin\theta/\lambda$, where θ and λ are the scattering angle and electron wavelength, respectively) was positioned at $s = 1.6 \text{ nm}^{-1}$ from the centre of each 40 nm ED pattern, corresponding to the 200 spot positions (inset, Fig. 2f).
- The mask underwent angular rotation through φ from -90° to 90° , with 0° defined as perpendicular to the stretching direction.
- A BG histogram was constructed from the integrated intensities within the circular mask for each ED pattern, with measurements performed at 1° intervals for $\varphi = -90^\circ$ to 90° (Fig. 2f). The BG histogram, representing the intensity distribution at positions devoid of the 200 spots, facilitated the discrimination between these spots and BG noise in the ED patterns.
- A maximum intensity histogram was constructed from the highest integrated intensities within the circular mask for each ED pattern, with measurements performed at 1° intervals for $\varphi = -90^\circ$ to 90° (Fig. 2f). This histogram characterised the intensities of the 200 spots.

The comparative analysis of these histograms revealed that weak 200 spots exhibited intensities comparable with those of certain BG signals. To identify the crystallite positions exhibiting 200 spots with 99.9% statistical confidence against BG noise, only the 40 nm ED

patterns in which the maximum intensities exceeded the 99.9th percentile of the BG histogram were selected. The positions of the 40 nm ED patterns with statistically significant 200 spots were mapped onto the ADF-STEM image (Fig. 2g).

FEM simulation

A FEM simulation was conducted to estimate the spatial distributions of local strain and stress. Elastic deformation was simulated using a modification of the method described in our previous study³⁸. The employed FEM simulator (PyMuffin Elastica (Version 0.91) in OCTA Version 8.4⁴⁸) was used to prepare the initial state based on the TEM image of silica-filled IR at $\varepsilon = 5.3$ and impose a uniaxial deformation up to $\varepsilon = 5.363$. The original TEM image at $\varepsilon = 5.3$ had a size of 1368×2274 pixels, with each pixel having a graduation of 256 levels. The TEM image was converted to a black/white binary image with a threshold value of 100 and then resized to 342×569 pixels. The two-dimensional image was triplicated in the thickness direction to form $342 \times 569 \times 3$ hexahedral mesh data, which were used as the input for the PyMuffin_Elastica simulator. A uniaxial deformation was performed from the size of $1 + 5.3$ to $1 + 5.363$ (net strain in the simulation was 0.01) by specifying the deformation at both ends of the system, while the boundaries in the other two directions were set free. We assumed an isotropic linear constitutive relation between the stress tensor σ_{ij} and strain tensor e_{ij} as

$$\sigma_{ij} = 2G(\mathbf{x}) \left\{ e_{ij} - \frac{1}{3} \delta_{ij} e_{\ell\ell} \right\} + K(\mathbf{x}) \delta_{ij} e_{\ell\ell}$$

where $G(\mathbf{x})$ and $K(\mathbf{x})$ are the bulk and shear moduli, respectively. Although the use of a linear constitutive relation may cause a quantitative error, this linear model grasped the essential features at a qualitative level³⁸.

The elastic moduli used in our previous study³⁸, that is, $K = 1950 \text{ MPa}$ and $G = 0.390 \text{ MPa}$ for the rubber (PI) matrix and $K = 38,000 \text{ MPa}$ and $G = 32,100 \text{ MPa}$ for the silica aggregates, were employed. The conjugate gradient method with an error level of 10^{-7} was used to solve the linear algebraic equation. The equilibrated data were processed to obtain the local displacement vectors, stress components, maximum and minimum stresses, and von Mises stress.

Data availability

All data are available from the corresponding author upon request.

Code availability

The code used for the analysis of the data in this study is available from the corresponding author upon request.

References

- Xu, S., Zhou, J. & Pan, P. Strain-induced multiscale structural evolutions of crystallized polymers: from fundamental studies to recent progresses. *Prog. Polym. Sci.* **140**, 101676 (2023).
- Auriemma, F., Alfonso, G. C. & De Rosa, C. *Polymer Crystallization II: From Chain Microstructure to Processing* (Springer Cham, 2017).
- Liu, C. et al. Tough hydrogels with rapid self-reinforcement. *Science* **372**, 1078–1081 (2021).
- Hashimoto, K. et al. Strain-induced crystallization and phase separation used for fabricating a tough and stiff slide-ring solid polymer electrolyte. *Sci. Adv.* **9**, eadi8505 (2023).
- Hartquist, C. M. et al. An elastomer with ultrahigh strain-induced crystallization. *Sci. Adv.* **9**, ead0411 (2023).
- Katz, J. R. Röntgenspektrographische Untersuchungen am gedehnten Kautschuk und ihre mögliche Bedeutung für das Problem der Dehnungseigenschaften dieser Substanz. *Naturwissenschaften* **13**, 410–416 (1925).

7. Katz, J. R. X-ray spectrography of polymers and in particular those having a rubber-like extensibility. *Trans. Faraday Soc.* **32**, 77 (1936).
8. Treloar, L. R. G. Rubbers and their characteristics: real and ideal. *Nature* **155**, 441–444 (1945).
9. Gent, A. N. Crystallization and the relaxation of stress in stretched natural rubber vulcanizates. *Trans. Faraday Soc.* **50**, 521–533 (1954).
10. Greibich, F. et al. Elastocaloric heat pump with specific cooling power of 20.9 W g⁻¹ exploiting snap-through instability and strain-induced crystallization. *Nat. Energy* **6**, 260–267 (2021).
11. Mark, H. & Susich, G. v. Ueber. Ueber geregelte Mizellarstrukturen von Kautschuk. *Kolloid Z.* **46**, 11–21 (1928).
12. Morss, H. A. Jr An X-ray study of stretched rubber. *Rubber Chem. Technol.* **11**, 352–358 (1938).
13. Bunn, C. W. Molecular structure and rubberlike elasticity. II. The stereochemistry of chain polymers. *Rubber Chem. Technol.* **15**, 731–741 (1942).
14. Nyburg, S. C. A statistical structure for crystalline rubber. *Acta Crystallogr.* **7**, 385–392 (1954).
15. Natta, G. & Corradini, P. Über die Kristallstrukturen des 1,4-cis-polybutadiens und des 1,4-cis-polyisoprens. *Angew. Chem.* **68**, 615–616 (1956).
16. Takahashi, Y. & Kumano, T. Crystal structure of natural rubber. *Macromolecules* **37**, 4860–4864 (2004).
17. Immirzi, A., Tedesco, C., Monaco, G. & Tonelli, A. E. Crystal structure and melting entropy of natural rubber. *Macromolecules* **38**, 1223–1231 (2005).
18. Rajkumar, G., Squire, J. M. & Arnott, S. A new structure for crystalline natural rubber. *Macromolecules* **39**, 7004–7014 (2006).
19. Che, J. et al. Crystal and crystallites structure of natural rubber and synthetic cis-1,4-polyisoprene by a new two dimensional wide angle X-ray diffraction simulation method. I. Strain-induced crystallization. *Macromolecules* **46**, 4520–4528 (2013).
20. Mark, J. E., Erman, B. & Roland, M. *The Science and Technology of Rubber* 4th edn (Academic Press, 2013). <https://doi.org/10.1016/C2011-0-05820-9>.
21. Rublon, P. et al. In situ synchrotron wide-angle X-ray diffraction investigation of fatigue cracks in natural rubber. *J. Synchrotron Radiat.* **20**, 105–109 (2013).
22. Zhou, W. et al. Toughening mystery of natural rubber deciphered by double network incorporating hierarchical structures. *Sci. Rep.* **4**, 7502 (2014).
23. Mai, T.-T. et al. Unraveling non-uniform strain-induced crystallization near a crack tip in natural rubber. *Adv. Sci.* **11**, e2307741 (2024).
24. Flory, P. J. Thermodynamics of crystallization in high polymers. I. Crystallization induced by stretching. *J. Chem. Phys.* **15**, 397–408 (1947).
25. Sotta, P. & Albouy, P. A. Strain-induced crystallization in natural rubber: Flory's theory revisited. *Macromolecules* **53**, 3097–3109 (2020).
26. Gent, A. N. & Zhang, L.-Q. Strain-induced crystallization and strength of rubber. *Rubber Chem. Technol.* **75**, 923–934 (2002).
27. Keller, A. & Machin, M. J. Oriented crystallization in polymers. *J. Macromol. Sci. B* **1**, 41–91 (1967).
28. Yeh, G. S. Y. & Hong, K. Z. Strain-induced crystallization, part III: Theory. *Polym. Eng. Sci.* **19**, 395–400 (1979).
29. Tosaka, M., Senoo, K., Sato, K., Noda, M. & Ohta, N. Detection of fast and slow crystallization processes in instantaneously-strained samples of cis-1,4-polyisoprene. *Polymer* **53**, 864–872 (2012).
30. Gros, A. et al. Dominating factor of strain-induced crystallization in natural rubber. *Polymer* **76**, 230–236 (2015).
31. Sun, S., Hu, F., Russell, T. P., Wang, D. & Zhang, L. Probing the structural evolution in deformed isoprene rubber by in situ synchrotron X-ray diffraction and atomic force microscopy. *Polymer* **185**, 121926 (2019).
32. Zhang, X. et al. Visualization and quantification of the microstructure evolution of isoprene rubber during uniaxial stretching using AFM nanomechanical mapping. *Macromolecules* **53**, 3082–3089 (2020).
33. Eggers, H. & Schummer, P. Reinforcement mechanisms in carbon black and silica loaded rubber melts at low stresses. *Rubber Chem. Technol.* **69**, 253–265 (1996).
34. Poompradub, S. et al. Mechanism of strain-induced crystallization in filled and unfilled natural rubber vulcanizates. *J. Appl. Phys.* **97**, 103529 (2005).
35. Chenal, J. M., Gauthier, C., Chazeau, L., Guy, L. & Bomal, Y. Parameters governing strain induced crystallization in filled natural rubber. *Polymer* **48**, 6893–6901 (2007).
36. Brüning, K., Schneider, K., Roth, S. V. & Heinrich, G. Kinetics of strain-induced crystallization in natural rubber studied by WAXD: dynamic and impact tensile experiments. *Macromolecules* **45**, 7914–7919 (2012).
37. Higuchi, T. et al. Development of a three-dimensional tomography holder for in situ tensile deformation for soft materials. *Microscopy* **67**, 296–300 (2018).
38. Miyata, T. et al. Nanoscale stress distribution in silica-nanoparticle-filled rubber as observed by transmission electron microscopy: implications for tire application. *ACS Appl. Nano Mater.* **4**, 4452–4461 (2021).
39. Miyata, T. et al. In-situ shearing process observation system for soft materials via transmission electron microscopy. *Microscopy* **73**, 208–214 (2024).
40. Panova, O. et al. Orientation mapping of semicrystalline polymers using scanning electron nanobeam diffraction. *Micron* **88**, 30–36 (2016).
41. Panova, O. et al. Diffraction imaging of nanocrystalline structures in organic semiconductor molecular thin films. *Nat. Mater.* **18**, 860–865 (2019).
42. Kanomi, S. et al. Nanodiffraction imaging of polymer crystals. *Macromolecules* **54**, 6028–6037 (2021).
43. Kanomi, S. et al. Reassessing chain tilt in the lamellar crystals of polyethylene. *Nat. Commun.* **14**, 5531 (2023).
44. Biran, I. et al. Transmission electron microscopy methodology to analyze polymer structure with submolecular resolution. *J. Phys. Chem. C* **128**, 5988–5995 (2024).
45. Chen, M. et al. Direct imaging of the crystalline domains and their orientation in the PS- b -PEO block copolymer with 4D-STEM. *Macromolecules* **57**, 5629–5638 (2024).
46. Kanomi, S., Azuma, K., Miyata, T., Toda, A. & Jinnai, H. Orientation distribution and branching mechanism of lamellar crystals inside an isotactic polystyrene spherulite. *Polymer* **326**, 128335 (2025).
47. Hjelle, Ø. & Dæhlen, M. Triangles and triangulations. *Mathematics and Visualization* 1–21 (Springer, 2006).
48. OCTA Website. Available from: <https://octa.jp/>.

Acknowledgements

This work was supported by the Japan Science and Technology Agency (JST) CREST (Grant Nos. JPMJCR2453 and JPMJCR1993 to H.J.) and the Japan Society for the Promotion of Science (JSPS) KAKENHI (Grant Nos. 20K15330 and 23H02017 to T.M. and 22H00329 to H.J.).

Author contributions

The manuscript was written with contributions from all authors. All authors approved the final version of the manuscript. T.M., S.K., K.C., and H.J. wrote the manuscript; D.W. and T.M. coordinated the experiments; W. M., T. Kikuchi, and T. Kitaura prepared rubber specimens; D.W. prepared TEM specimens and performed TEM observations and NDI measurements; D.W. and S.K. analysed TEM and NDI data; T. Kikuchi performed X-ray measurements; T. Kawakatsu contributed to FEM simulations; H.J. supervised the project.

Competing interests

The authors declare no competing interests.

Additional information

Supplementary information The online version contains supplementary material available at <https://doi.org/10.1038/s41467-025-63283-8>.

Correspondence and requests for materials should be addressed to Hiroshi Jinnai.

Peer review information *Nature Communications* thanks Xiaoke Mu and the other anonymous reviewer(s) for their contribution to the peer review of this work. A peer review file is available.

Reprints and permissions information is available at <http://www.nature.com/reprints>

Publisher's note Springer Nature remains neutral with regard to jurisdictional claims in published maps and institutional affiliations.

Open Access This article is licensed under a Creative Commons Attribution-NonCommercial-NoDerivatives 4.0 International License, which permits any non-commercial use, sharing, distribution and reproduction in any medium or format, as long as you give appropriate credit to the original author(s) and the source, provide a link to the Creative Commons licence, and indicate if you modified the licensed material. You do not have permission under this licence to share adapted material derived from this article or parts of it. The images or other third party material in this article are included in the article's Creative Commons licence, unless indicated otherwise in a credit line to the material. If material is not included in the article's Creative Commons licence and your intended use is not permitted by statutory regulation or exceeds the permitted use, you will need to obtain permission directly from the copyright holder. To view a copy of this licence, visit <http://creativecommons.org/licenses/by-nc-nd/4.0/>.

© The Author(s) 2025